An Improved Imaging Algorithm for HRWS Space-Borne SAR Data Processing Based on CVPRI

Yanan Guo, *Graduate Student Member, IEEE*, Pengbo Wang, *Member, IEEE*, Xinkai Zhou, *Graduate Student Member, IEEE*, Tao He, and Jie Chen, *Senior Member, IEEE*

***Abstract*—In space-borne synthetic aperture radar (SAR), the sliding spotlight mode can acquire images with both high-resolution and wide-swath in azimuth direction. Due to the significant two-dimensional spatial variance of Doppler parameters, the traditional imaging algorithms based on the conventional range models is not available. In this article, the strategy of continuously varying pulse repetition interval (CVPRI) is likely to lead to a novel approach to dealing with the azimuth variance problem to realize high-resolution wide-swath (HRWS) imaging in azimuth direction for sliding spotlight SAR. First, the eighth-order Taylor expansion of the modified equivalent squint range model (MESRM-TE8) is adopted, and the accuracy of MESRM-TE8 is accordingly explained. Then, the properties of the spatial variance for the MESRM-TE8 are analyzed in detail, based on which the strategy of CVPRI is given theoretically to eliminate the azimuth variance. An improved imaging algorithm based on CVPRI is subsequently proposed to address the azimuthal-variant Doppler parameters and realize a batch data processing of a large scene in azimuth frequency domain. The extended scaling method is integrated in this algorithm to uniformly compensate cubic phase modulation introduced by CVPRI and circumvent azimuth time folding caused by subaperture processing in the focused image. Finally, the effectiveness of the CVPRI strategy and the proposed algorithm is demonstrated by the simulation results.**

***Index Terms*—Continuously varying pulse repetition interval (CVPRI), high-resolution wide-swath (HRWS), imaging algorithm, sliding spotlight SAR, spatial variance, synthetic aperture radar (SAR).**

I. Introduction

SYNTHETIC aperture radar (SAR) is a powerful microwave remote sensing technique that can acquire the two-dimensional (2-D) images of the Earth's surface. Different from optical remote sensing, which passively utilizes sunlight as its illumination source, SAR relies on its own radiation and thus can adapt to bad weather and night environment. Because of these advantages, SAR has been highly valued in both civilian and military fields [1], [2]. Great progress has been made since the first space-borne SAR mission was launched in 1978 [3]. Nowadays, high-resolution wide-swath (HRWS) have become one of the most significant directions of SAR development [4], [5], [6], [7], [8], [9]. For example, the very high-resolution mode of the TerraSAR-X Next Generation (TSX-NG) mission will allow a spatial resolution of 0.25 m [10], [11]. Typically, the sliding spotlight mode [12], [13] is utilized to achieve the HRWS in space-borne SAR. For the sliding spotlight mode, "spotlight" allows a long synthetic aperture without excessively reducing the antenna length, whereas "sliding" allows a wide-swath in azimuth direction. In addition to the improvement of SAR sensor technology, the imaging algorithm should also be adopted to the HRWS condition. Generally, two challenges are faced in the HRWS space-borne SAR data processing. The first is the accurate formulation of the range history in a long integration time, and the second is the compensation of the 2-D spatial variance in Doppler parameters.

Due to the curvature of the satellite orbit and the rotation of the earth, the complex spatial geometry of HRWS space-borne SAR will lead to the failure of the traditional range models. The classical rang models assume that the platform moves along a straight track, such as the hyperbolic range equation model or the equivalent squint range model (ESRM) [14], [15]. These range models can properly formulate the relative slant range between the satellite platform and the scene center in the low and medium resolution cases. The fourth-order Doppler range model (DRM4) is then given a fourth-order polynomial function form to approximate the real range history in relatively high-resolution case [16], [17]. The polynomial function has a rather concise form which indicates the convenience for the derivation of 2-D spectrum and the analysis of spatial variance. However, in the very high-resolution space-borne SAR system, as the synthetic aperture time further increases, the fit between the real range history and the DRM4 range model drops rapidly. Therefore, the modified ESRM (MESRM) in [18] was developed by introducing the equivalent radar acceleration into the range equation. The first four-order terms and the higher-order terms of the real slant range can be described by MESRM accurately and partially, respectively. However, the root form of the MESRM range equation implies the inconvenience and the complexity of the spatial variance analysis. So, a range model with both accurate and brief form should be applied for the HRWS space-borne SAR imaging.

The 2-D spatial variance of the system is another serious challenge for the HRWS space-borne SAR data processing.

Manuscript received 12 July 2022; revised 11 October 2022 and 3 November 2022; accepted 15 November 2022. Date of publication 23 November 2022; date of current version 7 December 2022. This work was supported in part by the National Natural Science Foundation of China (NNSFC) under Grant 62101014, in part by the Shanghai Aerospace Science and Technology Innovation Foundation SAST2020-038, and in part by the National Natural Foundation of China under Grant U2241202. *(Corresponding author: Pengbo Wang.)*

The authors are with the School of Electronics and Information Engineering, Beihang University, Beijing 100191, China (e-mail: gyanan@buaa.edu.cn; wangpb7966@buaa.edu.cn; zhoux1nka1@buaa.edu.cn; tao_h@buaa.edu.cn; chenjie@buaa.edu.cn).

Digital Object Identifier 10.1109/JSTARS.2022.3224194

The conventional frequency domain imaging algorithms assume that the range history as well as the Doppler phase history of the targets appearing in the same range cell are identical, and therefore, the echoes of these targets can be focused via a bulk processing in the azimuth frequency domain. This assumption could be called "azimuthal-invariant." Commonly used algorithms include the range Doppler algorithm [19], [20], [21], the chirp scaling algorithm [22], [23], [24], etc. However, the premise of azimuth invariance is untenable for the HRWS space-borne SAR system working in sliding spotlight mode, which means the Doppler phase errors for the marginal targets will become non-negligible. The nonlinear chirp scaling (NCS) algorithm is a most widely adopted method in handling the azimuth variance problem [25], [26], [27], [28]. The main idea is utilizing a cubic phase perturbation to equalize the azimuth-varying Doppler parameters. High computational efficiency is its greatest advantage, which is attributed to the simple operation of eliminating azimuth variance by complex multiplication. However, the drawback is that an undesired azimuthal-variant linear term is introduced into the Doppler phase history, which results in a Doppler centroid frequency shift. This shift will lead to the mismatch of azimuth matched filtering and hence a degradation in the focusing precision for the marginal targets. Moreover, an azimuth resampling method was proposed to remove the azimuth variance in Doppler parameters [29], [30], [31]. The resampling method can alleviate the mismatch of the azimuth matched filtering, but the resampling process is relatively time-consuming and the truncation of the interpolation kernel will also cause losses in accuracy. In this article, a continuously varying pulse repetition interval (CVPRI) scheme is proposed to cope with the azimuth variance problem of the HRWS space-borne SAR. Instead of a constant PRI, the CVPRI scheme utilizes a specially designed time-varying PRI to compensate the azimuth variance of the Doppler parameters. The azimuthal-invariant SAR echo data can then be efficiently processed in the frequency domain. The CVPRI scheme can significantly reduce the Doppler spectrum shift and filter mismatch problems intrinsically introduced by the NCS algorithm, thus achieving higher focusing precision for the marginal targets.

This article begins with an analysis on the precision of the range models for the central point target under different spatial resolutions. The eighth-order Taylor expansion of MESRM (MESRM-TE8) is adopted according to the analysis to precisely formulate the range history for the HRWS space-borne SAR. Then, the spatial variance in azimuth direction is further analyzed for the MESRM-TE8, based on which the CVPRI strategy is accordingly put forward to compensate the azimuth variance. An improved hybrid correlation (HC) imaging algorithm, especially for the CVPRI scheme is then proposed. The accurate RCM correction and phase compensation are uniformly accomplished by an improved HC focusing processing for the full scene echo data. Ultimately, an extended scaling method is implemented to uniformly compensate the cubic phase term introduced by CVPRI and remove the azimuth time aliasing in the focused image. On the basis of spatial variance elimination by CVPRI strategy, the proposed imaging algorithm integrated with improved HC processing and extended scaling processing is utilized to complete high-resolution and high-precision batch imaging processing of the full scene echo data in Doppler frequency domain.

This article is organized as follows. In Section II, the analyses of the range model and signal model are explained. Additionally, the CVPRI strategy is also theoretically analyzed in this section. Section III illustrates the details of the improved HC algorithm based on CVPRI. Section IV presents the simulation results to demonstrate the effectiveness of the CVPRI strategy and the improved imaging algorithm. The conclusions are drawn in Section V.

II. Analyses of Range Model and Signal Model for Spatial-Variant System

A. Range Model Accuracy Analysis

For space-borne SAR, the accuracy of the range model is the premise of refined focusing. The MESRM model proposed in [18] is given by

$$R(t, r_0) = \sqrt{r_0^2 + v_0^2 t^2 - 2 r_0 v_0 t \cos\varphi_0 + \Delta a_3 t^3 + \Delta a_4 t^4} \tag{1}$$

where

$$\begin{cases} v_0 = \sqrt{\left(\frac{\lambda f_d}{2}\right)^2 - \frac{\lambda r_0 f_r}{2}} \\ \varphi_0 = \arccos\left(\frac{\lambda f_d}{2 v_0}\right) \\ \Delta a_3 = -\frac{\lambda r_0 f_{r3}}{6} - \frac{v_0^3 \sin^2\varphi_0 \cos\varphi_0}{r_0} \\ \Delta a_4 = -\frac{\lambda r_0 f_{r4}}{24} + \frac{v_0^4 \sin^2\varphi_0}{4 r_0^2}\left(1 - 5\cos^2\varphi_0\right) - \frac{\Delta a_3 v_0 \cos\varphi_0}{r_0} \end{cases} \tag{2}$$

where t is the azimuth slow time, r_0 is the slant range at the Doppler center time, v_0 is the equivalent velocity, φ_0 represents the equivalent squint angle, f_{r3} and f_{r4} denote the Doppler frequency modulation (FM) rate and its second-order derivative, respectively. For the target positioned at x_0 in azimuth direction, the beam-center-time is defined as t_0. The range history of this target can be formulated as $R(t, r_0, x_0) = R(t–t_0, r_0)$. The MESRM-TE8 for target positioned at x_0 is then could be expressed as follows:

$$R(t, r_0, x_0) = r_0 + \sum_{i=1}^{8} f_i (t - t_0)^i \tag{3}$$

where f_i, $\{i = 1, 2, 3, 4, 5, 6, 7, 8\}$ are eight expansion coefficients of the MESRM model in (1).

Fig. 1 shows the phase errors of the ESRM, DRM4, MESRM, and MESRM-TE8 as a function of azimuth time using the parameters listed in Table I. As can be observed from Fig. 1, the ESRM and the DRM4 range models will bring excessive phase errors with the increasing of synthetic aperture time, which is caused by the evident range deviations between the satellite platform and the scene center. By contrast, it can be noted that the MESRM and MESRM-TE8 range models are more accurate to formulate the actual range history. Even if the synthetic aperture time is up to 30 s, the maximum phase error of the MESRM range model is still less than the criteria of 0.25π, which can be explained by the terms from the fifth to eighth order in formula (3). The partial enlarged view in

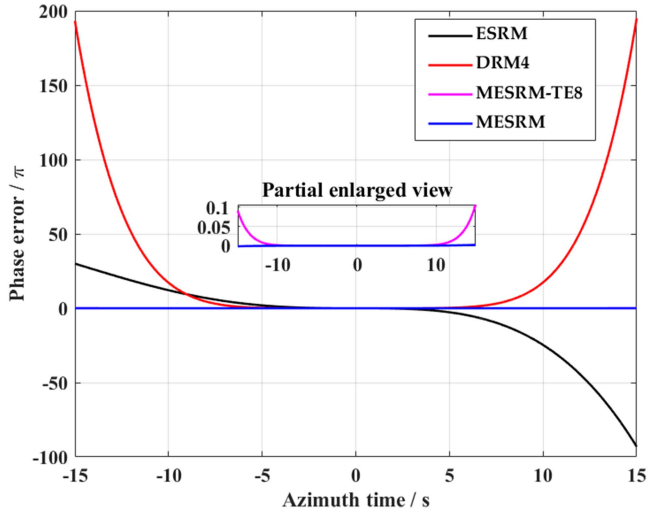

Fig. 1. Phase errors caused by range deviation as a function of azimuth time in ESRM/DRM4/MESRM/MESRM-TE-8.

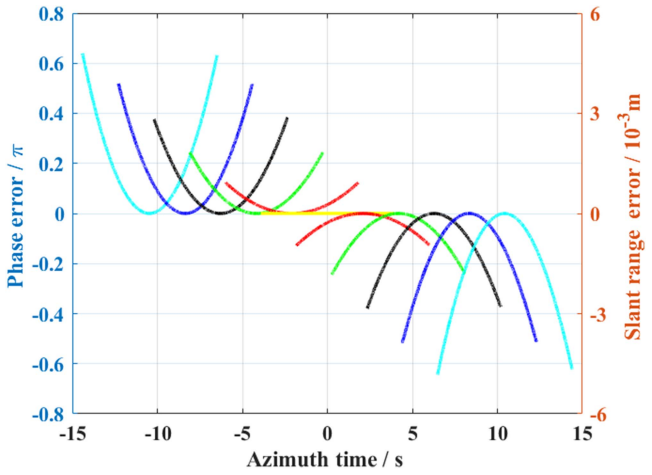

Fig. 2. Phase errors and the corresponding slant range errors as a function of azimuth time caused by MESRM-TE8. Lines with different colors represent the errors of different targets with a constant interval of 1 km along the azimuth dimension at the central range cell.

TABLE I
SIMULATION PARAMETERS

Description	Value	Units
Orbit altitude	514	km
Eccentricity	0.0011	–
Inclination	98.0	deg
Longitude of ascending node	0	deg
Argument of perigee	90	deg
Wavelength	0.03	m
Bandwidth	1.0	GHz
Sample frequency	1.5	GHz
PRF	4500	Hz
Look angle	30	deg
Antenna length	4.8	m
Squint angle	0	deg
Azimuth resolution	0.15	m
Hybrid factor	0.0625	–
Central latitude	45	deg

Fig. 1 illustrates that the MESRM-TE8 maintains the description accuracy of the MESRM range model. It can be found in [18] that all parameter in formula (1) in this article are determined by the first-order to fourth-order Doppler parameters, which means that the construction of the MESRM range model does not increase the accuracy requirements of the orbit, platform and other parameters in the radar system compared with the DRM4 range model. Therefore, the MESRM-TE8 model in (3) can ensure very high-resolution requirement without increasing the complexity of the system, which is attributed to the characteristics of the MESRM model. Besides, the polynomial form of the MESRM-TE8 facilitates the analysis of the spatial variance properties. As a result, the MESRM-TE8 is adopted in this article to approximate the actual range history.

B. Spatial Variance Analysis

Based on the selected rang model MESRM-TE8, the spatial variance analysis in azimuth dimension is given in this part by using the simulation parameters listed in Table I. Assuming that there are eleven targets, and they are located at the same range cell and uniformly distributed in the azimuth dimension with a constant interval of 1 km, which means the imaging swath in azimuth direction is set to be 10 km. The range deviations of these targets are then be simulated separately. Different from the stripmap mode, the rotation of the beam center in the sliding spotlight mode is also should be considered in the azimuth variance analysis of MESRM-TE8 range model. The phase errors and slant range errors of different targets are displayed in Fig. 2, which are caused by the range deviations between the real range histories and MESRM-TE8 range model. The azimuth slow time is the horizontal axis, while the phase errors and the corresponding slant range errors are represented by the left and right vertical axes, respectively.

As the distances from the scene center gradually increase in azimuth dimension, the phase errors increase as well as the corresponding slant range errors. For the marginal point targets located at 5 km away from the scene center, the absolute values of the maximum phase errors are approximately 0.65π as is shown in Fig. 2, which illustrates the degree of deterioration in the focusing quality for the edge points. Additionally, it should also be noted that the phase error of each point target is mainly composed by the quadratic term. After quantitative analysis, it is found that the amplitude of this quadratic term for each point target is almost proportional to its beam-center-time t_0. Therefore, the corresponding slant range error and the second-order Doppler parameter could be analytically related by

$$\Delta R\left(t, r_0, x_0\right) = \Delta f_2\left(t_0\right)\left(t - t_0\right)^2 \tag{4}$$

where $\Delta f_2\left(t_0\right)$ is the error of second-order Doppler parameter for target positioned at x_0. In order to limit the phase mismatch of the signal within 0.25π at any endpoint of the synthetic aperture, the amplitude of $\Delta f_2\left(t_0\right)$ should satisfy the following inequality:

$$\left|\Delta f_2\left(t_0\right)\right| \leq \frac{\lambda}{4} \cdot \frac{1}{T_s^2} \tag{5}$$

where $|\cdot|$ is an absolute value operator, T_s is the synthetic aperture time, and λ represents the signal wavelength of the

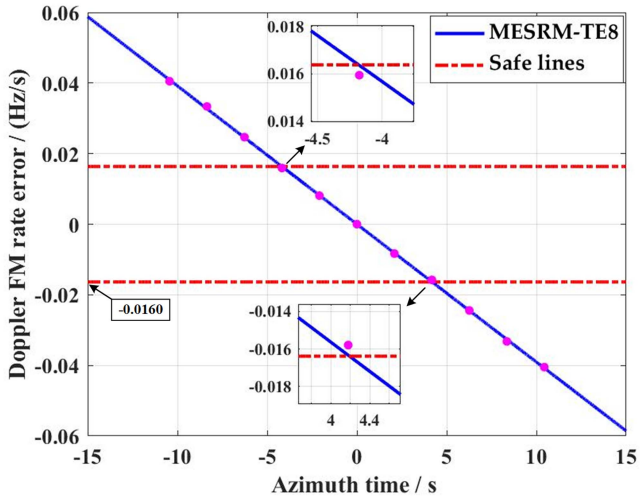

Fig. 3. Doppler FM rate error as a function of azimuth time caused by MESRM-TE8. The magenta dots denote the eleven targets evenly positioned along the azimuth dimension at the central range cell.

carrier. Furthermore, the Doppler FM rate error introduced by MESRM-TE8 is shown in Fig. 3. The fitting result in Fig. 3 indicates that the mapping relationship between $\Delta f_2\,(t_0)$ and the beam-center-time t_0 could be described as quasi-linear, which can be formulated as the following equation:

$$\Delta f_2\,(t_0) = \frac{\lambda}{4}\alpha\,(r_0)\,t_0 \tag{6}$$

where $\alpha\ (r_0)$ is the first-order fitting coefficient. Actually, $\alpha\ (r_0)$ is nearly range-invariant in the whole imaging scene, so it can then be simplified as α. The actual second-order Doppler parameter can then be modeled by

$$f_{2,actual}\,(t, r_0, x_0) = f_2\,(t, r_0, x_0) + \frac{\lambda}{4}\alpha t_0 \tag{7}$$

where $f_2\ (t,\ r_0,\ x_0)$ denotes the instantaneous second-order Doppler parameter of MESRM-TE8 at each azimuth time, which can be calculated by

$$f_2\,(t, r_0, x_0) = \frac{1}{2}\left\{\sum_{i=2}^{8}\left[i\,(i-1)\,f_i(t-t_0)^{i-2}\right]\right\}. \tag{8}$$

Besides, constrained by the maximum phase error of 0.25π, the maximum increment of $\Delta f_2\ (t_0)$ can be determined by formula (5). Then, the maximum azimuth imaging time range T_e could be approximately derived from the quasi-linear mapping relationship by formula (6). The corresponding imaging swath in azimuth dimension can then be approximately expressed as follows:

$$Sw_a = T_e v_g \tag{9}$$

where v_g represents the ground velocity of the antenna beam. It can be concluded that the effective azimuth imaging swath is nearly limited within 4 km as indicated by the red dotted lines in Fig. 3. Significant deterioration will happen for marginal targets due to the non-negligible errors of the second-order Doppler parameter.

C. Strategy of CVPRI

The azimuth signals generated by a group of point targets, which are laid on a given range cell, have azimuthal-variant Doppler FM rate. Therefore, it would be inaccurate to compress the whole azimuth signals using one single azimuth frequency domain matched filter, and the defocus phenomenon will occur for marginal targets. Since the azimuth variance is significant and almost range-invariant, the consistent azimuth variance compensation is necessary and feasible for imaging processing. Therefore, the CVPRI strategy is proposed to tackle this problem and subsequently realize HRWS data processing in azimuth frequency domain.

Assuming the relationship between the newly defined azimuth time η and the original azimuth time t could be formulated as follows:

$$\eta = t + \xi_1 t^2 \tag{10}$$

when the reference azimuth time is set to be zero for convenience. ξ_1 is the coefficient of the quadratic term. Thereafter, the slant range history can be expressed as follows:

$$R\,(\eta, r_0, x_0) = r_0 + \sum_{i=1}^{8} f_i(\eta - \eta_0)^i \tag{11}$$

where $\eta_0 = t_0 + \xi_1 t_0^2$. Only the analysis of the quadratic part for range history is sufficient to derive the scheme of CVPRI.

Substituting (10) into the quadratic term of the newly defined range history (11) and expanding the corresponding term (Appendix A), the quadratic term in (11) can be derived as follows:

$$f_2(\eta - \eta_0)^2 = f_2\,(1 + 4\xi_1 t_0)\,(t - t_0)^2 + 2f_2\xi_1(t - t_0)^3. \tag{12}$$

It could be found that ξ_1 is the primary azimuthal-variant component of the quadratic term. Additionally, a constant cubic modulation is introduced in the azimuth time domain, which will lead to obvious asymmetric side lobes for azimuth profile and should be considered in the imaging processing.

According to the previous analyses, the value of ξ_1 can be acquired by using the analytical fitting parameter in azimuth direction, which can be calculated by the following equation:

$$4f_2\xi_1 t_0 = \Delta f_2\,(t_0)\,. \tag{13}$$

In fact, there exists $f_2 = f_{2\_ref}$ at the reference range cell. Substituting (6) into (13) leads to the following relationship:

$$\xi_1 = \frac{\lambda}{16 f_{2\_ref}}\alpha. \tag{14}$$

Combine formula (10) with formula (14), the relation between η and t can be updated as follows:

$$\eta = t + \frac{\lambda}{16 f_{2\_ref}}\alpha t^2. \tag{15}$$

Due to the correlation between the newly defined azimuth time η and the original azimuth time t in (15), the relationship between the $(i+1)$th transmitted pulse interval PRI_{i+1} and the

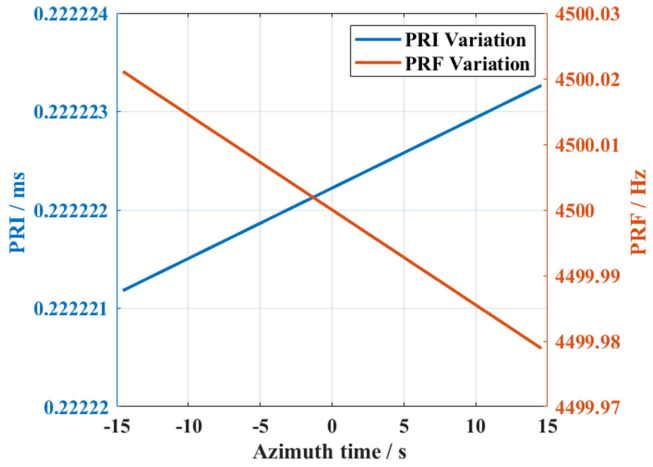

Fig. 4. Variation of PRI and PRF with respect to azimuth time.

*i*th transmitted pulse interval PRI_i can be revised as follows:

$$PRI_{i+1} = \frac{\lambda}{8f_{2\_ref}}\alpha \cdot \left(\frac{1}{PRF}\right)^2 + PRI_i \tag{16}$$

where *PRF* represents the pulse repetition frequency. Fig. 4 shows the PRI and PRF variation respecting to the azimuth time using parameters listed in Table I in Section IV-A. In order to simplify the illustration of CVPRI, the relationship between the instantaneous second-order Doppler parameter f'_2 and the azimuth time t when the rotating radar beam center points to the set target is shown in Fig. 5. By introducing CVPRI strategy, the azimuth sample positions keep changing and the dominant azimuthal-variant second-order Doppler parameter can be adjusted to be time-invariant, as in shown in Fig. 5. It is worth noting that the cubic phase and the high-order phase terms in formula (11) are almost immune to the CVPRI operation, and can be regarded as unaltered in the azimuth compression processing. Practically, when the squint angle approaches zero, the quadratic modulation phase in (A.1) introduced by the first-order term is so small that it could be ignored (Appendix A). In contrast, the continuous PRI variation has apparent influence on the second-order terms and should be considered seriously.

D. Signal Model Analysis

After introducing the data acquisition strategy of CVPRI, the signal model of the system is accordingly altered. Based on the newly defined slant range history in (11), the received signal after down-converting to baseband could be expressed in terms of the range time and azimuth time as follows:

$$S(\tau,\eta) = \sigma_0\omega_a(\eta-\eta_0)\exp\left\{-j\frac{4\pi}{\lambda}R(\eta)\right\} \cdot\omega_r\left(\tau-\frac{2R(\eta)}{c}\right)\exp\left\{j\pi K_r\left[\tau-\frac{2R(\eta)}{c}\right]^2\right\} \tag{17}$$

where $R(\eta)$ is the new slant range history of signal received via the CVPRI data acquisition strategy, σ_0 is the scattering coefficient, c is the propagation speed of light, τ is the fast time in range direction, K_r represents the chirp rate of the transmitted signal, $\omega_a(\cdot)$ and $\omega_r(\cdot)$ denote the antenna pattern functions in the azimuth and range directions, respectively. The difference from the traditional signal model is that the newly defined azimuth time is nonuniform as illustrated in formulas (10) and (15). Therefore, the influence of CVPRI strategy on the 2-D spectrum is mainly reflected in the history of slant range.

The signal in range frequency domain, using the POSP method, can be derived as follows:

$$S(f_\tau,\eta) = \sigma_0\omega_r(f_\tau)\exp\left\{-j\frac{\pi}{K_r}f_\tau^2\right\} \cdot\omega_a(\eta-\eta_0)\exp\left\{-j\frac{4\pi(f_c+f_\tau)}{c}R(\eta)\right\}. \tag{18}$$

Then, the POSP method combined with the series reversion (MSR) [32] is applied to derive an accurate 2-D point target spectrum (PTS) based on the CVPRI strategy, which can be obtained as follows:

$$S(f_\tau,f_a) = \sigma_0\omega_a(\eta_a(f_a,f_\tau))\cdot\omega_r(f_\tau) \cdot\exp\left\{-j4\pi\left(\frac{f_c+f_\tau}{c}\right)\left(r_0+\sum_{i=1}^{8}f_i\eta_a^i(f_a,f_\tau)\right)\right\} \cdot\exp\left\{-j2\pi f_a\eta_a(f_a,f_\tau)\right\}\cdot\exp\left\{-j\frac{\pi}{K_r}f_\tau^2\right\} \tag{19}$$

where

$$\eta_a(f_a,f_\tau) = t_a(f_a,f_\tau) + \xi_1 t_a^2(f_a,f_\tau) \tag{20}$$

where f_a and f_τ represent the azimuth and range frequency, respectively, and f_c is carrier frequency. $t_a(f_a,f_\tau)$ is the stationary phase point and could be derived from the following equation:

$$2\left(\frac{f_c+f_\tau}{c}\right)\frac{\partial R(t_a(f_a,f_\tau))}{\partial t} + f_a = 0. \tag{21}$$

By solving formula (21), the azimuth frequency f_a and the original azimuth time t are now related by

$$t_a(f_a,f_\tau) = t'_a\left(f_a+\frac{2(f_c+f_\tau)}{c}f_1,f_\tau\right) \tag{22}$$

$$t'_a(f_a,f_\tau) = \sum_{i=2}^{7}A_iP(f_a,f_\tau)^{i-1}, P(f_a,f_\tau) = -\frac{cf_a}{2(f_c+f_\tau)} \tag{23}$$

where

$$\begin{cases} A_2 = 1.0/a_2 \\ A_3 = (-a_3)/a_2^3 \\ A_4 = \left(2a_3^2 - a_2a_4\right)/a_2^5 \\ A_5 = \left(-a_5a_2^2 + 5a_4a_3a_2 - 5a_3^3\right)/a_2^7 \\ A_6 = \left(-a_6a_2^3 + \left(3a_4^2+6a_3a_5\right)a_2^2 - 21a_3^2a_4a_2 + 14a_3^4\right)/a_2^9 \\ A_7 = \begin{pmatrix}(7a_3a_6+7a_4a_5)a_2^3 - 28\left(a_5a_3^2+a_3a_4^2\right)a_2^2 \\ +84a_3^3a_4a_2 - 42a_3^5 - a_7a_2^4\end{pmatrix}\Big/a_2^{11} \end{cases} \tag{24}$$

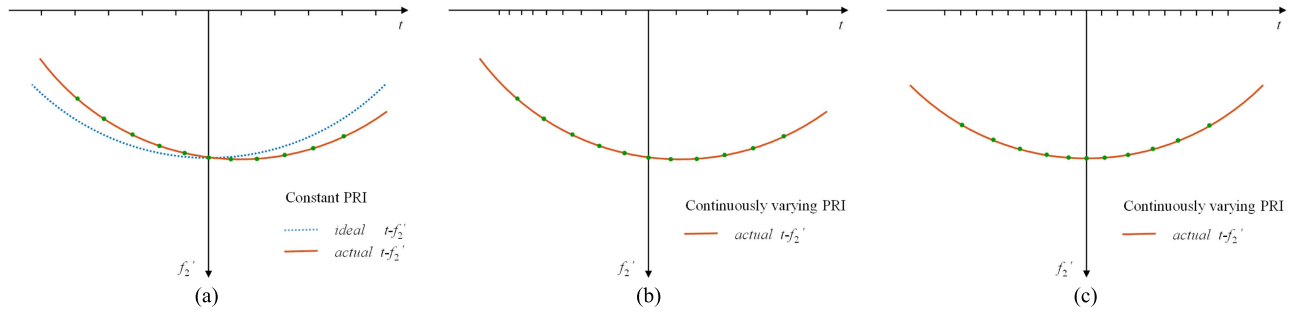

Fig. 5. (a) Ideal and actual relationships between the azimuth time t and the instantaneous second-order Doppler parameter f'_2 when the constant PRI is adopted. (b) Linear azimuth variance correction of f'_2 by using CVPRI strategy. (c) Result of linear azimuth variance correction of f'_2 after using CVPRI strategy. The green dots identify the eleven targets evenly positioned along the azimuth direction at the central range cell.

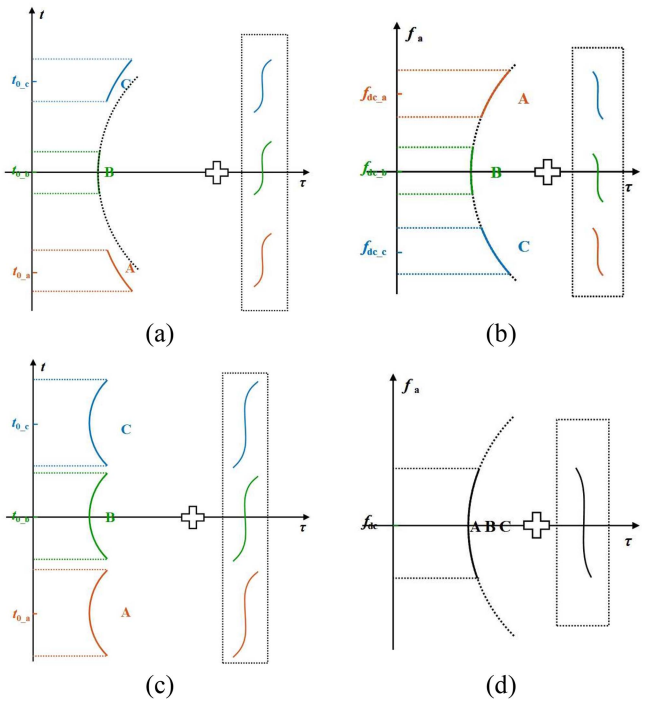

Fig. 6. Range history when working in sliding spotlight mode in (a) 2-D time domain and (b) range Doppler domain. The range history when working in stripmap mode in (c) 2-D time domain and (d) range Doppler domain. Lines with different colors represent the range history of targets distributed in different azimuth positions at the central range cell.

In formula (24), $a_i = i \cdot f_i$, where i represents the number from 2 to 7. Substituting (20) into (19), the desired 2-D PTS can be acquired. The accuracy of the spectrum formulated in (19) is limited by the number of terms used in (23), and its high precision will be verified in subsequent simulation experiments.

In Section II-C, it is noted that the second term in (12) is a cubic phase modulation, which is caused by the scheme of CVPRI and consistent for all targets. Fig. 6 illustrates the difference of range history when the satellite works in sliding spotlight mode (a)-(b) and stripmap mode (c)-(d). Due to the introduction of CVPRI strategy, a cubic term is added to the slant range histories in both the 2-D time domain and range Doppler domain, as shown in the right part of each subpicture.

Fig. 6(a) and (c) explain that the cubic phase terms are completely consistent in 2-D time domain for differently positioned point targets whether the system operates in sliding spotlight mode or stripmap mode. By comparing Fig. 6(b) and (d), it can be noticed that the cubic terms of differently positioned point targets have identical amplitude no matter which mode the system works in. However, in the azimuth frequency domain, there are still some differences in the cubic terms for different operating modes. Different point targets occupy different azimuth spectrum ranges for the sliding spotlight mode shown in Fig. 6(b), whereas an identical azimuth spectrum scope is occupied for stripmap mode shown in Fig. 6(d).

Accordingly, for the edge point target, when working in sliding spotlight mode, the azimuth signal associated with the introduced cubic term can be written as follows:

$$h_{3th}(t-t_0) = \omega_a(t-t_0)\exp\{j2\pi f_{dc}(t-t_0)\} \cdot \exp\left\{-j\pi\frac{\alpha}{2}(t-t_0)^3\right\} \quad (25)$$

where f_{dc} is the Doppler centroid frequency for the edge target. Applying an azimuth Fourier transform (FT) to the signal in (25), the Doppler signal of the edge point target becomes

$$H_{3th}(f_a) = \omega_a(t_a(f_a)) \cdot \exp\{-j2\pi f t_0\} \cdot \exp\left\{-j\pi\frac{\alpha}{2}t^3(f_a - f_{dc})\right\} \quad (26)$$

where $t_a(f_a)$ represent the azimuth stationary phase point. Combined Fig. 6 with formula (26) for analysis, the introduced cubic phase terms for different targets are distinguished by distinct f_{dc} in the azimuth frequency dimension.

III. Improved HC Algorithm Based on CVPRI

The analyses of range model and signal model for spatial-variant system have been displayed in Section II, and simultaneously, the strategy of CVPRI is also exhibited to eliminate the complex azimuth variance. An efficient imaging algorithm is then proposed here for the HRWS space-borne SAR data processing working in sliding spotlight mode.

In order to handle the azimuth spectrum aliasing issue caused by the insufficient PRF, two methods, namely, the two-step processing method [33] and the subaperture method [13], [18], are

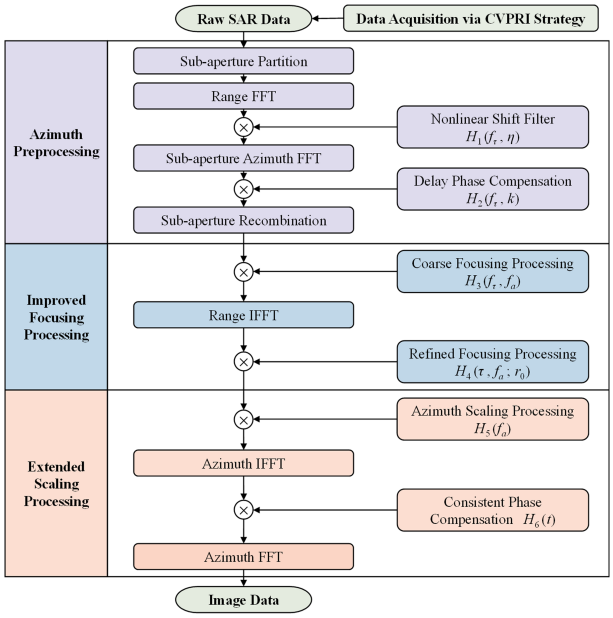

Fig. 7. Block diagram of the proposed algorithm.

usually implemented. According to [21] and [33], the two-step method is inappropriate for ultrahigh-resolution case, which is limited by the transmitted bandwidth. Hence, the subaperture method in [18] is selected as the azimuth preprocessing method here. Then, the improved focusing algorithm based on the MESRM-TE8 rang model is proposed to correct the whole RCM and compensate the corresponding Doppler phase, which will achieve the high-precision focusing within the full wide-swath, and the range compression is also fulfilled at the same time. Owing to the increased azimuth sampling rate caused by azimuth preprocessing, the azimuth time axis in focused imaging may be compressed, and subsequently, imaging aliasing would arise. In addition, it could be observed from Section II-D that the constant cubic phase modulation introduced by CVPRI is distributed in different azimuth frequency bands, thus increasing the difficulty of unified compensation processing operation. Therefore, in the last step, an extended scaling method is put forward and employed in this article to compensate the cubic phase term caused by CVPRI and eliminate the azimuth time aliasing caused by subaperture processing in focused image. There is some analogy with the method which is used in [34], where the two-step method is utilized to overcome spectrum aliasing.

The block diagram of the improved HC algorithm is revealed in Fig. 7. In the subsequent sections, each major stage of the improved HC algorithm will be analyzed and discussed in the following.

A. Azimuth Preprocessing

In the sliding spotlight mode, the whole azimuth bandwidth is much larger than PRF. The subaperture method is exploited here to remove the spectrum aliasing caused by the beam steering. First, the whole echo signal is divided into several subapertures. After each echo partition is transformed into the range frequency domain by performing a range fast Fourier transform (FFT), the nonlinear shift filtering is employed, which is given by

$$H_1(f_\tau, \eta) = \exp\left\{-j2\pi \left\lfloor \left(1 + \frac{f_\tau}{f_c}\right) f_{d,k} T_{sub} \right\rfloor \frac{f_{prf}}{N_{sub}} \eta \right\} \tag{27}$$

where $\lfloor \cdot \rfloor$ is rounding down operation of an element, T_{sub} is the size of subaperture, N_{sub} is the azimuth samples in each subaperture, and f_{prf} and $f_{d,k}$ denote the azimuth sampling rate and the kth subaperture's Doppler centroid frequency, respectively.

Then, the FFT in azimuth direction is implemented for each subaperture. The 2-D spectrum of the echo signal can be acquired without Doppler spectrum aliasing through the recombination of each subaperture and the compensation of the time delay phase. The compensation function of time delay phase is given as follows:

$$H_2(f_\tau, k) = \exp\left\{-j2\pi \left\lfloor \left(1 + \frac{f_\tau}{f_c}\right) f_{d,k} T_{sub} \right\rfloor \frac{f_{prf}}{N_{sub}} \eta_k \right\} \tag{28}$$

where η_k is the kth subaperture's center time.

B. Improved Focusing Processing

After adopting the data acquisition strategy of CVPRI, the consistent azimuth variance compensation has been accomplished. The azimuth matched filtering can then be implemented in range Doppler domain by the improved HC focusing processing proposed in this article to realize the whole RCM correction and Doppler phase compensation. The traditional HC algorithm cannot meet the requirement of efficient imaging processing in the case of HRWS in azimuth direction [19]. Therefore, the entire focusing processing should be divided into two parts: the coarse focusing processing and the refined focusing processing, to maintain a balance between precision and efficiency. The details of the focusing processing are described as follows.

The coarse focusing processing is conducted by multiplying an azimuth reference function which is constructed by the Doppler parameters in the central range cell, so as to remove the bulk RCM, Doppler phase modulation, and the high-order cross-coupling. The azimuth reference function can be described as follows:

$$H_3(f_\tau, f_a) = \exp\left\{j2\pi f_a \eta_{a\_ref}(f_a, f_\tau)\right\} \cdot \exp\left\{j\frac{\pi}{K_r} f_\tau^2\right\} \cdot \exp\left\{j4\pi \left(\frac{f_c + f_\tau}{c}\right) \left(\sum_{i=1}^{8} f_{i\_ref} \eta_{a\_ref}^i(f_a, f_\tau)\right)\right\} \tag{29}$$

where f_{i_ref} represents the Doppler parameters in the reference range cell and $\eta_{a\_ref}(f_a, f_\tau)$ denotes the corresponding stationary phase point, which is given by

$$\begin{cases} \eta_{a\_ref}(f_a, f_\tau) = t_{a\_ref}(f_a, f_\tau) + \xi_1 t_{a\_ref}^2(f_a, f_\tau) \\ t_{a\_ref}(f_a, f_\tau) = t_{a\_ref}{}'\left(f_a + \frac{2(f_c + f_\tau)}{c} f_{1\_ref}, f_\tau\right) \end{cases} \tag{30}$$

where the subscript *ref* represents the reference range cell, which usually defaults to the central range cell. Note that the coarse focusing has been fulfilled together with range matched filtering after the inverse FFT (IFFT) along the range direction.

There only exists differential RCM and Doppler phase modulation in range Doppler domain for noncentral range cells. Thus, it is of necessity to employ the HC processing in range Doppler domain to address these problems.

The kernel length of the sliding window decreases rapidly since the bulk RCM of the noncentral range cells has been removed. The "sliding window" refers to the 2-D reference function constructed to realize azimuth matched filtering, which is updated in range direction. By updating the reference function along the range cell, the refined focusing processing can be efficiently accomplished by HC operation. For the i_{r0}th range cell, the signal after HC processing becomes

$$S_1(i_{r_0}, f_a) = \sum_{i=-m/2+1}^{m/2} S(i + i_{r_0}, f_a) \cdot H_4(i, f_a; r_0) \tag{31}$$

$$H_4(i, f_a; r_0) = Disc\left[conj\left(FT_R^{-1}(H_4(f_\tau, f_a; r_0))\right)\right] \tag{32}$$

where m is the sliding window length, $Disc[\cdot]$ is the discrete representation of reference function, $conj(\cdot)$ is complex conjugate processing of the signal, $FT_R^{-1}(\cdot)$ represents the rang inverse FFT (IFFT), $S(i+i_{r0}, f_a)$ is the echo signal in range Doppler domain for the $i+i_{r0}$th range cell that has completed the coarse focusing processing, $H_4(f_\tau, f_a; r_0)$ denotes the reference function updated along the range cell, which is constructed in 2-D frequency domain, and is given by

$$\begin{aligned} H_4(f_\tau, f_a; r_0) = & \exp\left\{j4\pi\left(\frac{f_c + f_\tau}{c}\right)\left(\sum_{i=1}^{8} f_i {\eta_a}^i(f_a, f_\tau)\right)\right\} \\ & \cdot \exp\left\{-j4\pi\left(\frac{f_c + f_\tau}{c}\right)\right. \\ & \left.\times\left(\sum_{i=1}^{8} f_{i\_ref} {\eta_{a\_ref}}^i(f_a, f_\tau)\right)\right\}. \end{aligned} \tag{33}$$

The step size of the reference function updating along the range direction and the length of the sliding window need to be determined according to the application requirements.

C. Extended Scaling Processing

As is analyzed in Section II-D, the compensation of cubic phase modulation caused by CVPRI in sliding spotlight mode is more complicated than that in stripmap, since the different Doppler centroid frequency of each point target positioned at a given range cell. The unified cubic phase compensation can be accomplished in azimuth frequency domain only if these targets occupy identical frequency band, which could be incorporated into the Doppler phase compensation processing in Section III-B. Therefore, an extended scaling method is carried out here to uniformly compensate the cubic phase term, accompanied by the elimination of time domain aliasing caused by subaperture.

Continuing with the formula (26), neglecting the constant phase terms and the negligible nonuniformity of the azimuth sampling time in the subsequent derivation, the residual azimuth signal after Doppler phase compensation in Section III-B can be rewritten as follows:

$$\begin{aligned} S_{res}(f_a) = & rect\left(\frac{f_a - f_{dc}}{B_a}\right)\exp\left\{-j2\pi f_a\left(t_0 - \frac{f_{dc}}{f_r}\right)\right\} \\ & \cdot \exp\left\{j\pi\frac{\alpha}{2}\left(\frac{f_a - f_{dc}}{f_r}\right)^3\right\} \end{aligned} \tag{34}$$

where B_a is the Doppler bandwidth of a point target, and f_r is the Doppler FM rate.

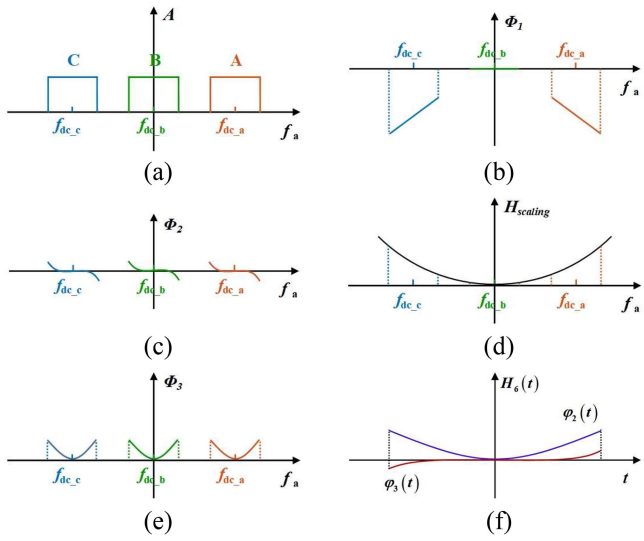

Fig. 8. (a) Spectrum amplitude of the azimuth signal after matched filtering. (b) Linear Doppler phase modulation of the azimuth signal after matched filtering. (c) Cubic Doppler phase modulation of the azimuth signal after matched filtering. (d) Scaling function along the azimuth direction. (e) Quadratic phase modulation introduced by scaling operation. (f) Residual phase terms in the dual domain of Doppler domain.

Fig. 8 shows the principle of uniformly compensating the cubic phase using scaling method. It is assumed that targets A, B, and C lie at the same range cell but different azimuth positions. Fig. 8(a) shows the spectral position and the amplitude of the echo signal after compression using a frequency domain matched filter. Fig. 8(b) and (c) display the corresponding linear and cubic phase terms of each azimuth signal, respectively. The three linear phases have different slopes, which are closely related to the corresponding azimuth positions of these targets, whereas the cubic terms in Doppler domain are identical for these targets. The scaling function is given a quadratic form to compensate the linear phase originating from displacement in azimuth direction, which is shown in Fig. 8(c). This quadratic phase is added to the linear phase in (b) along the azimuth frequency to offset the position shift. Subsequently, the extra and uniform quadratic terms shown in Fig. 8(e) are introduced. When transformed into the dual domain, both the cubic and the quadratic terms take up the same time scope as is shown in Fig. 8(f), which indicates that the consistent compensation is achievable for them. Besides, the azimuth time folding in the focused image, which is caused by the subaperture processing in azimuth direction, can also be circumvented simultaneously.

To determine the quadratic phase term of the scaling function, the specific derivation is given in Appendix B. The scaling

function is introduced to compensate the linear phase in (34), and it is given by

$$H_5(f_a) = \exp\left\{j\pi \frac{f_a^2}{k_e}\right\} \tag{35}$$

$$k_e = \frac{\gamma \cdot f_{r,rot}}{H_f} \tag{36}$$

where k_e is the scaling factor as denoted in (36), γ is calculated by formula (B.5) in Appendix B and H_f represents the hybrid factor, which can be expressed as follows:

$$H_f = \frac{r_{rot} - r_0}{r_{rot}} \tag{37}$$

where r_{rot} is the distance from the rotation point to the radar sensor at the Doppler center time.

After complex multiplication with (35), omitting the constant amplitude of the spectrum, the signal in (34) changes into

$$S_{res1}(f_a) = rect\left(\frac{f_a - f_{dc}}{B_a}\right)\exp\left\{j\pi\frac{(f_a - f_{dc})^2}{k_e}\right\} \cdot \exp\left\{j\pi\frac{\alpha}{2}\left(\frac{f_a - f_{dc}}{f_r}\right)^3\right\}. \tag{38}$$

Next, IFFT along the azimuth direction is performed, the signal is then transformed into the dual domain and can be written as follows:

$$F^{-1}\left(S_{res1}(f_a)\right) = rect\left(\frac{k_e t}{B_a}\right)\exp\left\{j2\pi f_{dc} t\right\} \cdot \exp\left\{-j\pi k_e t^2\right\}\exp\left\{-j\pi\frac{\alpha}{2}\left(\frac{k_e}{f_r}\right)^3 t^3\right\}. \tag{39}$$

All target signals at a given range cell will occupy a unified azimuth time scope.

Considering the additional quadratic phase introduced by the scaling processing, the filter of the consistent phase compensation can be described as follows:

$$H_6(t) = \exp\left\{j\pi k_e t^2\right\} \cdot \exp\left\{j\pi\frac{\alpha}{2}\left(\frac{k_e}{f_{r\_ref}}\right)^3 t^3\right\} \tag{40}$$

where f_{r_ref} is the Doppler FM rate of the reference range cell. Finally, after an azimuth FFT, the uniform cubic phase compensation and azimuth time de-aliasing can be completed. All the scatters in the scene can be well focused without azimuth time folding.

IV. Simulation Example

To verify the imaging ability of the improved HC algorithm based on CVPRI for HRWS space-borne sliding spotlight SAR, a simulation using the parameters given in Table I is carried out. An array of 9 targets is used in this simulation, and they are laid out on a square area of 10 km × 10 km in ground range/azimuth, as is shown in Fig. 9. The intervals of different targets are 5 km and the rectangular windows are assumed in both the range and azimuth dimensions.

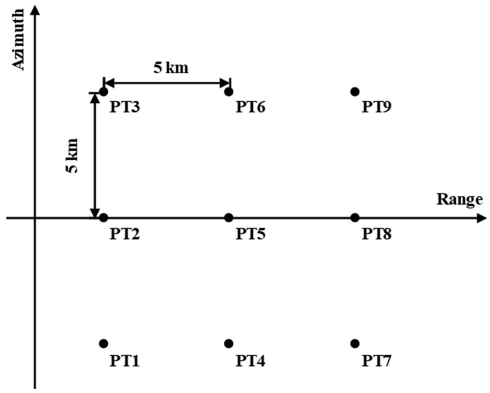

Fig. 9. Ground scene layout of the point targets in the simulation.

A. Simulation Results

The simulation results of the echo data received by the CVPRI strategy and processed by the improved HC algorithm are displayed in Figs. 10 and 11, whereas the results of the NCS algorithm proposed in [25], [26], [27], and [28] for comparison are shown in Figs. 12 and 13.

The simulation results before employing the CVPRI strategy are represented by the 2-D contours shown in Fig. 10(a) and the blue dashed lines shown in Fig. 11. It could be seen that the reference central point target (PT5) is well focused, and the azimuth profile is identical with the theoretical profile, while the edge point targets (PT1 and PT9) 5 km away from the center of the scene suffer from significant quality deterioration in both azimuth profiles and 2-D contours. The above-mentioned phenomenon is also identical with the analyses shown in Section II-B, because of the considerable phase errors introduced by the severe mismatch of the second-order Doppler parameter. The azimuth focusing performance will be seriously degraded, including non-negligible azimuth main-lobe broadening and side-lobe arising. After introducing the data receiving strategy of CVPRI and the improved HC algorithm, the quality of the imaging results is improved significantly compared with the results before using the CVPRI strategy. The 2-D contours shown in Fig. 10(b) and the black dotted lines shown in Fig. 11 represent the simulation results of the proposed algorithm before the extended scaling processing. It can be observed that apparent side-lobe asymmetry phenomenon arises with the elimination of the azimuth spatial variance after adopting the CVPRI strategy. There is somewhat similar with the NCS algorithm, in which this problem may not have been settled so far. The black dotted lines shown in Fig. 11 indicate that the amplitude of the first side-lobes on both sides differ by approximately 2.0 dB because of the additional cubic phase modulation. After applying extended scaling processing, the difference is reduced considerably and limited within 0.3 dB, which can be seen from the red solid lines shown in Fig. 11.

The 2-D contours shown in Fig. 12 and blue dashed lines shown in Fig. 13 verify that most of the quadratic phase errors could been removed when using the NCS algorithm to eliminate the azimuth spatial variance. In fact, with the elimination of azimuth variance in Doppler parameters, additional phase terms

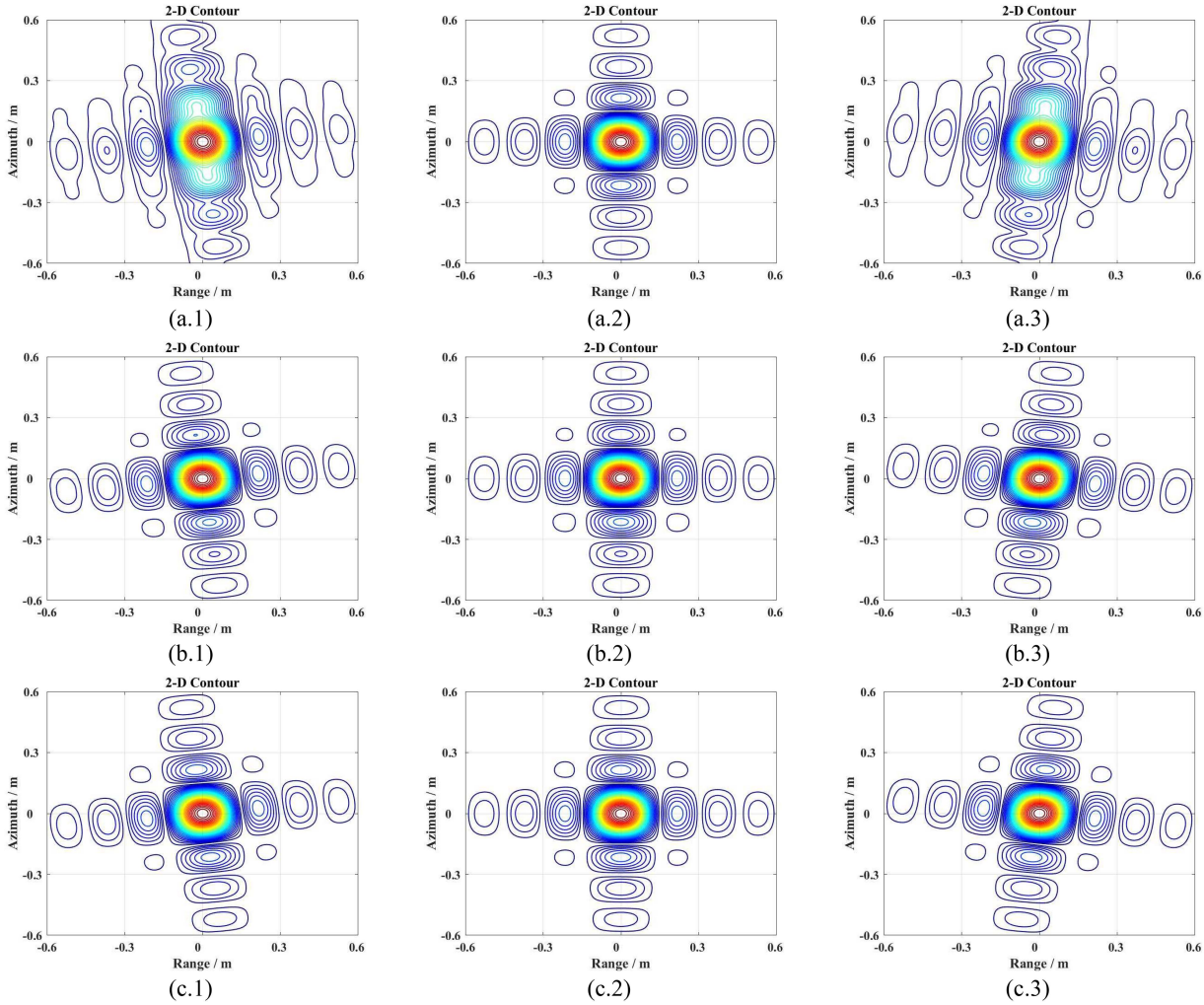

Fig. 10. Evaluated results of the 2-D contours for the chosen targets. (x.1)–(x.3) Results of targets PT1, PT5 and PT9 shown in Fig. 9, respectively. (a) Results before CVPRI. (b) Results before extended scaling processing. (c) Results after extended scaling processing.

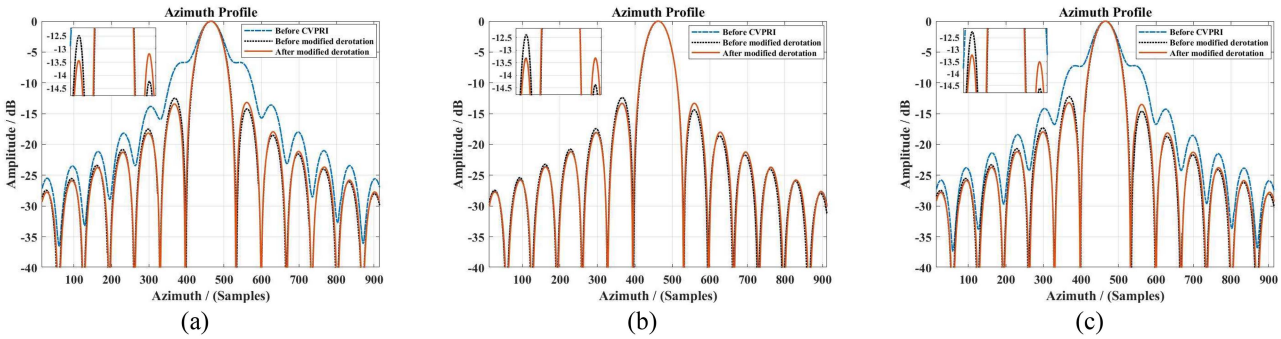

Fig. 11. Evaluated results of the azimuth profiles for the chosen targets. (a)–(c) Results of targets PT1, PT5, and PT9 shown in Fig. 9, respectively. The blue dashed lines, the black dotted lines and the red solid lines denote the results before CVPRI, before extended scaling processing, and after extended scaling processing, respectively.

will be introduced, mainly containing the extra cubic phase modulation and the azimuthal-variant Doppler spectrum shift, which will become obvious for HRWS space-borne sliding spotlight SAR system. The cubic phase term introduced by NCS algorithm is complicated to be uniformly compensated and cannot be incorporated into azimuth phase compensation in Section III-B. It could lead to asymmetric side-lobes as is shown in Figs. 12 and 13. Besides, there is still a certain degree of adhesion in side-lobes for the 2-D contours as is displayed in Fig. 12, which is caused by the Doppler spectrum shift. Compared the NCS method to the CVPRI strategy, the contours of main-lobe and subsequent side-lobes shown in Fig. 10(b) and (c) are obviously

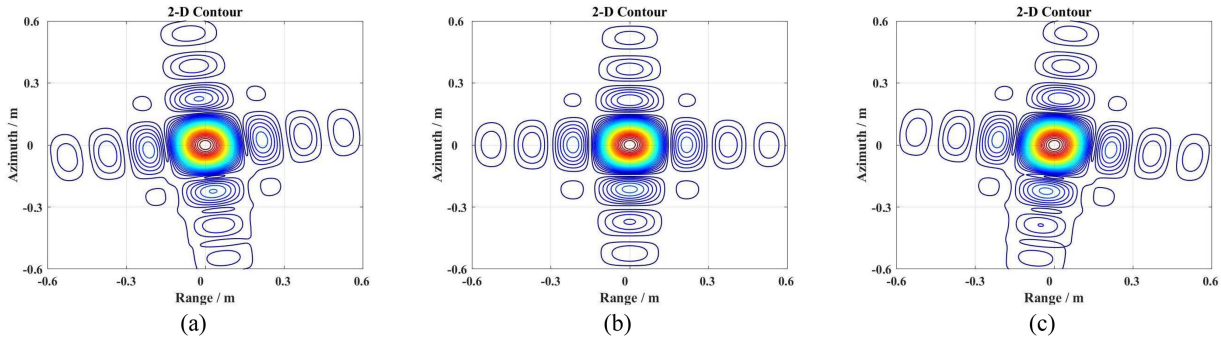

Fig. 12. Evaluated results of the 2-D contours for the chosen targets after using the NCS algorithm. (a)–(c) Results of targets PT1, PT5, and PT9 shown in Fig. 9, respectively.

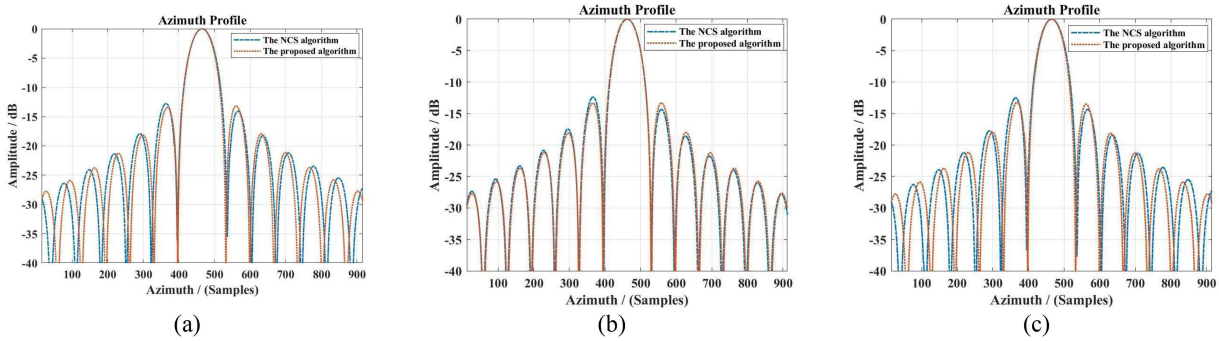

Fig. 13. Evaluated results of azimuth profiles for the chosen targets. (a)–(c) Results of targets PT1, PT5, and PT9 shown in Fig. 9, respectively. The blue dashed lines and the red dotted lines denote the results after using the NCS algorithm and the proposed algorithm, respectively.

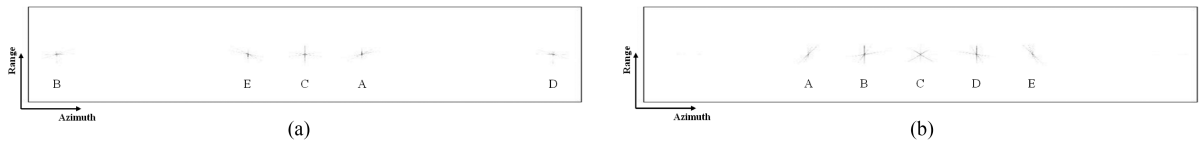

Fig. 14. (a) Results before eliminating azimuth time domain aliasing in the focused image. (b) Results after eliminating azimuth time domain aliasing in the focused image.

separated from each other, which is attributed to the fact that the Doppler spectrum shift introduced by CVPRI strategy is much smaller than that of the NCS method.

Additionally, in order to explain the time de-aliasing, effectiveness of the extended scaling processing, five points targets are evenly distributed along the azimuth direction at a constant interval of 2.5 km. The results before and after azimuth time de-aliasing in the focused image are shown in Fig. 14(a) and (b), respectively. Then, it can be confirmed that the cubic phase modulation introduced by CVPRI strategy and the azimuth time folding caused by the subaperture could be eliminated simultaneously when using the extended scaling processing.

The imaging performances of all targets shown in Fig. 9 are displayed in Table II from a quantitative point of view. The symbols $\rho_{a,c}$ and $\rho_{r,c}$ denote the ideal resolution values in azimuth and range directions, respectively. When the rectangular antenna patterns are assumed both in range and azimuth directions, the theoretical PSLR and ISLR in these two dimensions are -13.26 dB and -9.68 dB, respectively. All targets are well focused in range dimension—the range PSLR deviates less than 0.05 dB from the theoretical value, and the range ISLR is within 0.22 dB from the expected value. The imaging results for all targets in azimuth dimension have been significantly improved—the azimuth broadening is less than 2.0%, and the PSLR and ISLR have degradations of less than 0.1 dB and 0.9 dB from the ideal values, respectively.

Overall, the imaging performances have been improved significantly after using the data acquisition strategy of CVPRI and the improved HC algorithm based on CVPRI.

B. Computational Burden

Suppose the final image with full resolution has N_r range samples and N_a azimuth samples. The computational complexity of the proposed algorithm and the reference algorithm in [28] is compared in Table III. The length of the HC sliding window is K_1 and the Doppler parameters are updated every K_2 range cells in this article. From the flowchart in Fig. 7, it can be obtained that

TABLE II
IMAGING PERFORMANCE OF NINE POINT TARGETS

Target	Azimuth					Range				
	ρ_a (m)	$\rho_{a,c}$ (m)	IRW	PSLR (dB)	ISLR (dB)	ρ_r (m)	$\rho_{r,c}$ (m)	IRW	PSLR (dB)	ISLR (dB)
1	0.144	0.142	1.41%	−13.19	−10.46	0.133	0.133	0.00%	−13.31	−9.86
2	0.142	0.142	0.70%	−13.31	−10.52	0.135	0.133	1.50%	−13.27	−9.86
3	0.144	0.142	1.41%	−13.21	−10.47	0.134	0.133	0.75%	−13.27	−9.87
4	0.134	0.133	0.75%	−13.20	−10.54	0.134	0.133	0.75%	−13.28	−9.90
5	0.133	0.133	0.00%	−13.32	−10.51	0.134	0.133	0.75%	−13.28	−9.90
6	0.134	0.133	0.75%	−13.20	−10.56	0.134	0.133	0.75%	−13.26	−9.89
7	0.126	0.124	1.61%	−13.19	−10.53	0.134	0.133	0.75%	−13.25	−9.86
8	0.126	0.124	1.61%	−13.31	−10.48	0.135	0.133	1.50%	−13.25	−9.89
9	0.126	0.124	1.61%	−13.20	−10.34	0.135	0.133	1.50%	−13.26	−9.76

TABLE III
ANALYSIS OF COMPUTATIONAL COMPLEXITY

Operation	The proposed algorithm	The reference algorithm
Times of range FT	2	4
Times of azimuth FT	3	3
Times of complex multiplication	5	9
Times of HC	1	0

the total computational complexity of the proposed algorithm is

$$\left(\frac{3}{2}\log_2(N_a)+\log_2(N_r)\right)N_aN_r+5N_aN_r+K_1\cdot N_a\cdot\frac{N_r}{K_2}$$
$$=\left(\frac{3}{2}\log_2(N_a)+\log_2(N_r)+5+\frac{K_1}{K_2}\right)N_aN_r. \quad (41)$$

The HC sliding window length K_1 and the updated step length of Doppler parameters K_2 are chosen as 32 and 2, respectively, to maintain satisfactory accuracy. The computational complexities of the proposed algorithm and the reference algorithm can then be summarized in (42) and (43), respectively.

$$\left(\frac{3}{2}\log_2(N_a)+\log_2(N_r)+21\right)N_aN_r \quad (42)$$

$$\left(\frac{3}{2}\log_2(N_a)+2\log_2(N_r)+9\right)N_aN_r. \quad (43)$$

Assuming $N_a=N_r=N$, the computational complexities of them could be simplified as follows:

$$\left(\frac{5}{2}\log_2(N)+21\right)N^2 \quad (44)$$

$$\left(\frac{7}{2}\log_2(N)+9\right)N^2. \quad (45)$$

The computational complexities of the two algorithms with respect to number of samples are simulated and shown in Fig. 15, which indicates a slight computational burden improvement of the proposed algorithm under the premise of ensuring high focusing performance within the full swath.

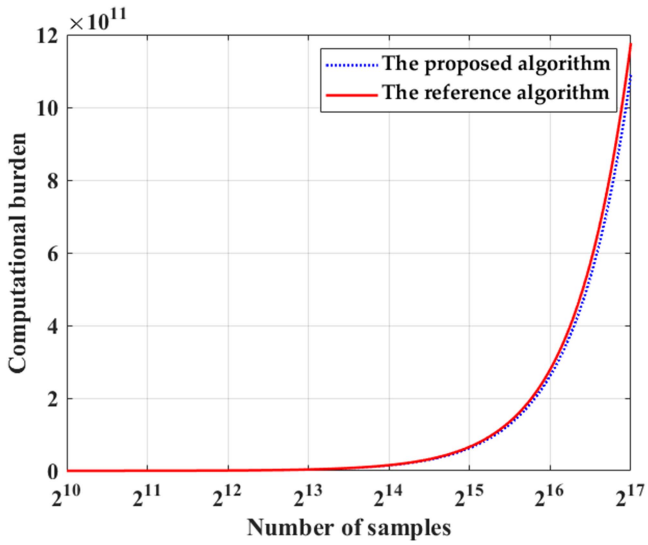

Fig. 15. Comparison of computational burden for the proposed algorithm and the reference algorithm.

C. Discussion

The major error of the imaging algorithm is mainly introduced by the elimination processing of the azimuth variance, especially in large squint mode, which determines its maximum applicable swath width in azimuth dimension.

It is noted that the linear term of the newly defined range history (Appendix A) brings the extra phase terms. Neglecting the extremely slight quadratic phase modulation, an extra small spatially varying Doppler centroid frequency shift is introduced in the echo signal, which is given by

$$\Delta f_{d\_1}(r_0,x_0)=\frac{f_1}{4f_{2\_ref}}\alpha t_0. \quad (46)$$

When the NCS method is used to equalize the second-order Doppler parameter, the corresponding Doppler centroid frequency shift could be described as follows:

$$\Delta f_{d\_2}(r_0,x_0)=-\frac{\alpha}{2}t_0^2. \quad (47)$$

Naturally, a mismatch on the RCM correction will be caused by the Doppler centroid frequency shift, which is correspondingly given by

$$\Delta RCM = \frac{\lambda}{2}\Delta f_d T_s. \tag{48}$$

Under the requirement that ΔRCM does not need to be corrected, the safe line of the RCM error usually be set as follows:

$$\Delta RCM \le \frac{\rho_r}{4} \tag{49}$$

where ρ_r is the spatial resolution in range direction. The maximum azimuth swath in azimuth direction is limited by the set safe line of the RCM correction. Define the ration of ΔRCM and ρ_r as κ, then κ can be denoted as follows:

$$\kappa = \frac{\Delta RCM}{\rho_r}. \tag{50}$$

With the simulation parameters in Table I, the values of κ caused by NCS method and CVPRI strategy are approximately 0.17 and 4.05×10^{-5}, respectively. By comparison, it reveals that ΔRCM introduced by CVPRI strategy is rather smaller than that caused by the NCS method. The effective scene in azimuth direction should be limited within 11.2 km when using the NCS method, which can be calculated in (48) and (49). The ΔRCM can be ignored within tens of kilometers in azimuth direction in this article when CVPRI scheme is adopted. Beyond that, the influence of the azimuthal-variant Doppler centroid frequency shift on azimuth matched filtering is significant and complicated. Constrained by the phase error of 0.25π, it is found via simulation that the proposed algorithm can still show well performance when the azimuth swath reaches 14 km under the premise that the range and azimuth resolution requirements are both 0.15 m. To summarize, the CVPRI strategy shows great advantages since the slight Doppler centroid frequency shift caused by it, especially in the condition of a wider swath in azimuth direction. These analyses can be confirmed by the simulation results shown in Section IV-A. For space-borne sliding spotlight SAR system with large squint angle, the Doppler centroid frequency shift caused by CVPRI strategy may should be taken into serious consideration.

V. Conclusion

For HRWS space-borne SAR system working in sliding spotlight mode, the conventional imaging algorithms based on the traditional range models is not adaptable due to the significant 2-D spatial variance of the Doppler parameters. The CVPRI strategy is proposed in this article as a novel approach to resolve the azimuth variance of the system. In comparison with the existing spatial variance compensation methods, the CVPRI method guarantees the processing accuracy while taking the efficiency into account. First, the MESRM-TE8 range model is adopted to precisely describe the range history of the scene targets. The properties of the spatial-variant system are also analyzed for MESRM-TE8, based on which the strategy of the CVPRI is used to eliminate the azimuth variance in Doppler parameters. An improved HC algorithm based on CVPRI strategy is then proposed in this article. The improved HC focusing processing is employed to realize the total RCM correction and precise phase compensation, which keeps a balance between the focusing accuracy and efficiency. Subsequently, an extended scaling method corresponding to subaperture approach is performed to uniformly compensate the cubic phase modulation introduced by CVPRI strategy and simultaneously circumvent the azimuth time folding in the focused image. The simulation results verify the effectiveness of the CVPRI strategy and the proposed imaging algorithm.

Appendix A

Substituting (10) into the first-order to fourth-order slant range terms of (11), these terms can be written as follows:

$$\begin{aligned} f_1(\eta-\eta_0) &= f_1\left(\left(t+\xi_1 t^2\right)-\left(t_0+\xi_1 t_0^2\right)\right) \\ &= f_1\left(1+2\xi_1 t_0\right)(t-t_0)+f_1\xi_1(t-t_0)^2. \end{aligned} \tag{A.1}$$

In this article, the quadratic term introduced by f_1 (η–η_0) is rather smaller, and so could be neglected during the compensation processing.

$$\begin{aligned} f_2(\eta-\eta_0)^2 &= f_2\left(\left(t+\xi_1 t^2\right)-\left(t_0+\xi_1 t_0^2\right)\right)^2 \\ &= f_2\Big((t-t_0)^2+\xi_1^2(t^2-t_0^2)^2+2\xi_1(t-t_0)(t^2-t_0^2)\Big). \end{aligned} \tag{A.2}$$

Owing to the quantity of ξ_1 is relatively small, the square term of ξ_1 in (A.2) has little influence on the modulation phase, and can be omitted in the following analysis. The residual terms that contribute significantly to the modulation phase can be expressed as follows:

$$f_2(\eta-\eta_0)^2 = f_2\left((t-t_0)^2+2\xi_1\left(t-t_0\right)\left(t^2-t_0^2\right)\right). \tag{A.3}$$

Expanding (A.3) at $t = t_0$ leads to

$$f_2(\eta-\eta_0)^2 = f_2\Big((t-t_0)^2+2\xi_1(t-t_0)\Big((t-t_0)^2+2t_0(t-t_0)\Big)\Big). \tag{A.4}$$

After classifying each order term in (A.4), formula (10) can be obtained.

Appendix B

The linear phase of the point target after further refined focusing is written down as follows. Later, the quadratic coefficient of the scaling function is selected in such a way that the linear phase modulation could be removed.

The discrete form of the linear phase of the echo signal for a point target should be

$$\Phi_{a\_linear} = \exp\left\{-j2\pi n_1 \Delta f_{a\_1} t'_0\right\}, t'_0 = t_0 - \frac{f_{dc}}{f_r} \tag{B.1}$$

where n_1 represents integers from $-N_b/2$ to $N_b/2$, N_b is the number of the FFT points after zero-padding, and Δf_{a_1} is the corresponding frequency resolution in azimuth direction and can be expressed as follows:

$$\Delta f_{a\_1} = \frac{f_{prf\_deramp}}{N_b} \tag{B.2}$$

where f_{prf_deramp} is the equivalent sampling rate in azimuth direction when the de-ramp method in [33] is adopted to compensate the extra Doppler bandwidth caused by antenna steering, and it could be given by

$$f_{prf\_deramp} = \frac{N_b \cdot f_{r,rot}}{f_{prf}} \tag{B.3}$$

where $f_{r,rot}$ is the slope of the varied Doppler centroid frequency.

However, when using subaperture method to relieve the contradiction between the Doppler bandwidth and PRF, the new frequency resolution becomes

$$\Delta f_{a\_2} = \frac{\gamma \cdot f_{r.rot}}{f_{prf}} \tag{B.4}$$

$$\gamma = \frac{N_{burst} \cdot f_{prf}^2}{N_a \cdot f_{r,rot}} \tag{B.5}$$

where N_{burst} is the number of the subapertures, and N_a is the azimuth point number of the final image. Naturally, the linear phase in discrete form could be altered as follows:

$$\Phi_{a\_linear} = \exp\left\{-j2\pi n_2 \Delta f_{a\_2} t_0^{''}\right\} \tag{B.6}$$

where n_2 represents integers from $-N_a/2$ to $N_a/2$. The new azimuth position is carried out by comparing formula (B.2) with (B.4), which is given by

$$t''_0 = \frac{1}{\gamma}\left(t_0 - \frac{f_{dc}}{f_r}\right). \tag{B.7}$$

REFERENCES

[1] A. Moreira, P. Prats-Iraola, M. Younis, G. Krieger, I. Hajnsek, and K. P. Papathanassiou, "A tutorial on synthetic aperture radar," *IEEE Geosci. Remote Sens. Mag.*, vol. 1, no. 1, pp. 6–43, Mar. 2013.

[2] F. Ma, F. Zhang, D. Xiang, Q. Yin, and Y. Zhou, "Fast task-specific region merging for SAR image segmentation," *IEEE Trans. Geosci. Remote Sens.*, vol. 60, 2022, Art. no. 5222316.

[3] W. Townsend, "An initial assessment of the performance achieved by the Seasat-1 radar altimeter," *IEEE J. Ocean. Eng.*, vol. 5, no. 2, pp. 80–92, Apr. 1980.

[4] M. Villano, G. Krieger, and A. Moreira, "Staggered SAR: High-resolution wide-swath imaging by continuous PRI variation," *IEEE Trans. Geosci. Remote Sens.*, vol. 52, no. 7, pp. 4462–4479, Jul. 2014.

[5] D. Cerutti-Maori, I. Sikaneta, J. Klare, and C. H. Gierull, "MIMO SAR processing for multichannel high-resolution wide-swath radars," *IEEE Trans. Geosci. Remote Sens.*, vol. 52, no. 8, pp. 5034–5055, Aug. 2014.

[6] F. Q. de Almeida, M. Younis, G. Krieger, and A. Moreira, "New slow PRI variation scheme for multichannel SAR high-resolution wide-swath imaging," in *Proc. IEEE Int. Geosci. Remote Sens. Symp.*, 2018, pp. 3655–3658.

[7] F. Q. de Almeida, M. Younis, P. Prats-Iraola, M. Rodriguez-Cassola, G. Krieger, and A. Moreira, "Slow pulse repetition interval variation for high-resolution wide-swath SAR imaging," *IEEE Trans. Geosci. Remote Sens.*, vol. 59, no. 7, pp. 5665–5686, Jul. 2021.

[8] Y. Wang, Z. Ding, P. Xu, K. Chen, T. Zeng, and T. Long, "Strip layering diagram-based optimum continuously varying pulse interval sequence design for extremely high-resolution spaceborne sliding spotlight SAR," *IEEE Trans. Geosci. Remote Sens.*, vol. 59, no. 8, pp. 6751–6770, Aug. 2021.

[9] Y. Zhou et al., "High-resolution and wide-swath SAR imaging mode using frequency diverse planar array," *IEEE Geosci. Remote Sens. Lett.*, vol. 18, no. 2, pp. 321–325, Feb. 2021.

[10] J. Janoth, S. Gantert, T. Schrage, and A. Kaptein, "Terrasar next generation—Mission capabilities," in *Proc. IEEE Int. Geosci. Remote Sens. Symp.*, 2013, pp. 2297–2300.

[11] J. Janoth, M. Jochum, L. Petrat, and T. Knigge, "High resolution wide swath—The next generation X-band mission," in *Proc. IEEE Int. Geosci. Remote Sens. Symp.*, 2019, pp. 3535–3537.

[12] J. Mittermayer, R. Lord, and E. Boerner, "Sliding spotlight SAR processing for TerraSAR-X using a new formulation of the extended chirp scaling algorithm," in *Proc. IEEE Int. Geosci. Remote Sens. Symp.*, 2003, pp. 1462–1464.

[13] P. Prats, R. Scheiber, J. Mittermayer, A. Meta, and A. Moreira, "Processing of sliding spotlight and TOPS SAR data using baseband azimuth scaling," *IEEE Trans. Geosci. Remote Sens.*, vol. 48, no. 2, pp. 770–780, Feb. 2010.

[14] X. Sun, T. S. Yeo, C. Zhang, Y. Lu, and P. S. Kooi, "Time-varying stepttransform algorithm for high squint SAR imaging," *IEEE Trans. Geosci. Remote Sens.*, vol. 37, no. 6, pp. 2668–2677, Nov. 1999.

[15] J. Mittermayer, A. Moreira, and O. Loffeld, "Spotlight SAR data processing using the frequency scaling algorithm," *IEEE Trans. Geosci. Remote Sens.*, vol. 37, no. 5, pp. 2198–2214, Sep. 1999.

[16] K. Eldhuset, "A new fourth-order processing algorithm for spaceborne SAR," *IEEE Trans. Aerosp. Electron. Syst.*, vol. 34, no. 3, pp. 824–835, Jul. 1998.

[17] K. Eldhuset, "Spaceborne bistatic SAR processing using the EETF4 algorithm," *IEEE Geosci. Remote Sens. Lett.*, vol. 6, no. 2, pp. 194–198, Apr. 2009.

[18] P. Wang, W. Liu, J. Chen, M. Niu, and W. Yang, "A high-order imaging algorithm for high-resolution spaceborne SAR based on a modified equivalent squint range model," *IEEE Trans. Geosci. Remote Sens.*, vol. 53, no. 3, pp. 1225–1235, Mar. 2015.

[19] C. Wu, K. Y. Liu, and M. Jin, "Modeling and a correlation algorithm for spaceborne SAR signals," *IEEE Trans. Aerosp. Electron. Syst.*, vol. AES-18, no. 5, pp. 563–575, Sep. 1982.

[20] R. Bamler, "A comparison of range-Doppler and wavenumber domain SAR focusing algorithms," *IEEE Trans. Geosci. Remote Sens.*, vol. 30, no. 4, pp. 706–713, Jul. 1992.

[21] P. Wang, W. Liu, J. Chen, M. Niu, and W. Yang, "A high-order imaging algorithm for high-resolution spaceborne SAR based on a modified equivalent squint range model," *IEEE Trans. Geosci. Remote Sens.*, vol. 53, no. 3, pp. 1225–1235, Mar. 2015.

[22] R. K. Raney, H. Runge, R. Bamler, I. G. Cumming, and F. H. Wong, "Precision SAR processing using chirp scaling," *IEEE Trans. Geosci. Remote Sens.*, vol. 32, no. 4, pp. 786–799, Jul. 1994.

[23] A. Moreira and Y. Huang, "Airborne SAR processing of highly squinted data using a chirp scaling approach with integrated motion compensation," *IEEE Trans. Geosci. Remote Sens.*, vol. 32, no. 5, pp. 1029–1040, Sep. 1994.

[24] A. Moreira, J. Mittermayer, and R. Scheiber, "Extended chirp scaling algorithm for air- and spaceborne SAR data processing in stripmap and ScanSAR imaging modes," *IEEE Trans. Geosci. Remote Sens.*, vol. 34, no. 5, pp. 1123–1136, Sep. 1996.

[25] F. H. Wong, I. G. Cumming, and Y. L. Neo, "Focusing bistatic SAR data using the nonlinear chirp scaling algorithm," *IEEE Trans. Geosci. Remote Sens.*, vol. 46, no. 9, pp. 2493–2505, Sep. 2008.

[26] L. Huang, X. Qiu, D. Hu, B. Han, and C. Ding, "Medium-earth-orbit SAR focusing using range Doppler algorithm with integrated two-step azimuth perturbation," *IEEE Geosci. Remote Sens. Lett.*, vol. 12, no. 3, pp. 626–630, Mar. 2015.

[27] G.-C. Sun, M. Xing, Y. Wang, J. Yang, and Z. Bao, "A 2-D space-variant chirp scaling algorithm based on the RCM equalization and subband synthesis to process geosynchronous SAR data," *IEEE Trans. Geosci. Remote Sens.*, vol. 52, no. 8, pp. 4868–4880, Aug. 2014.

[28] Z. Men, P. Wang, J. Chen, C. Li, W. Liu, and W. Yang, "Advanced high-order nonlinear chirp scaling algorithm for high-resolution wide-swath spaceborne SAR," *Chin. J. Aeronaut.*, vol. 34, no. 2, pp. 563–575, Feb. 2021.

[29] Y. Wu, G.-C. Sun, C. Yang, J. Yang, M. Xing, and Z. Bao, "Processing of very high resolution spaceborne sliding spotlight SAR data using velocity scaling," *IEEE Trans. Geosci. Remote Sens.*, vol. 54, no. 3, pp. 1505–1518, Mar. 2016.

[30] G. Sun, Y. Wu, J. Yang, M. Xing, and Z. Bao, "Full-aperture focusing of very high resolution spaceborne-squinted sliding spotlight SAR data," *IEEE Trans. Geosci. Remote Sens.*, vol. 55, no. 6, pp. 3309–3321, Jun. 2017.

[31] W. Liu, G.-C. Sun, X.-G. Xia, J. Chen, L. Guo, and M. Xing, "A modified CSA based on joint time-Doppler resampling for MEO SAR stripmap mode," *IEEE Trans. Geosci. Remote Sens.*, vol. 56, no. 6, pp. 3573–3586, Jun. 2018.

[32] Y. L. Neo, F. H. Wong, and I. G. Cumming, "Processing of azimuth-invariant bistatic SAR data using the range Doppler algorithm," *IEEE Trans. Geosci. Remote Sens.*, vol. 46, no. 1, pp. 14–21, Jan. 2008.

[33] R. Lanari, M. Tesauro, E. Sansosti, and G. Fornaro, "Spotlight SAR data focusing based on a two-step processing approach," *IEEE Trans. Geosci. Remote Sens.*, vol. 39, no. 9, pp. 1993–2004, Sep. 2001.

[34] W. Yang, J. Chen, W. Liu, P. Wang, and C. Li, "A modified three-step algorithm for TOPS and sliding spotlight SAR data processing," *IEEE Trans. Geosci. Remote Sens.*, vol. 55, no. 12, pp. 6910–6921, Dec. 2017.

Yanan Guo (Graduate Student Member, IEEE) was born in 1996. She received the B.S. degree in communication engineering from Wuhan University of Science and Technology, Wuhan, Hubei, China, in 2018. She is currently working toward the Ph.D. degree with Beihang University (Beijing University of Aeronautics and Astronautics, BUAA), Beijing, China.

Her research interests include high-resolution SAR image formation and azimuthal multiangle SAR image formation.

Pengbo Wang (Member, IEEE) was born in 1979. He received the Ph.D. degree in information and communication engineering from Beihang University, Beijing, China, in 2007.

From 2007 to 2010, he held a Postdoctoral position with the School of Electronics and Information Engineering, Beihang University. From 2014 to 2015, he was a Visiting Researcher with the Department of Electronic and Electrical Engineering, University of Sheffield, Sheffield, U.K. Since 2015, he has been an Associate Professor with the School of Electronics and Information Engineering, Beihang University. His research interests include high-resolution spaceborne SAR image formation, novel techniques for spaceborne SAR systems, and multimodal remote sensing data fusion.

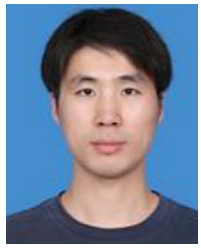

Xinkai Zhou (Graduate Student Member, IEEE) received the B.S. degree in electronic engineering and the M.S. degree in information and communication engineering from Beihang University, Beijing, China, where he is currently working toward the Ph.D. degree in signal and information processing.

His research interests include active/passive SAR image formation and passive radar target detection.

Tao He was born in Chengdu, China, in 1998. He received the B.S. degree from Chengdu University of Information Technology, Chengdu, China, in 2020. He is currently working toward the Ph.D. degree in signal and information processing in electronic engineering with Beihang University, Beijing, China.

His research interests include novel techniques for SAR system, high-resolution spaceborne SAR image formation, and passive radar signal processing.

Jie Chen (Senior Member, IEEE) was born in 1973. He received the B.S. and Ph.D. degrees in information and communication engineering from Beihang University, Beijing, China, in 1996 and 2002, respectively.

Since 2004, he has been an Associate Professor with the School of Electronics and Information Engineering, Beihang University. He was a Visiting Researcher with the School of Mathematics and Statistics, University of Sheffield, Sheffield, U.K., from 2009 to 2010, working on ionospheric effects on low-frequency space radars that measure forest biomass and ionospheric electron densities. Since July 2011, he has been a Professor with the School of Electronics and Information Engineering, Beihang University. His research interests include multimodal remote sensing data fusion, topside ionosphere exploration with spaceborne HF/VHF-synthetic aperture radar (SAR) systems, and high-resolution spaceborne SAR image formation and SAR image quality enhancement.